Materials and Design 188 (2020) 108477

Contents lists available at ScienceDirect

Materials and Design

journal homepage: www.elsevier.com/locate/matdes

High-temperature Laves precipitation and its effects on recrystallisation behaviour and Lüders deformation in super ferritic stainless steels

Hui-Hu Lu [a], Hong-Kui Guo [a], Wei Liang [a,*], Jian-Chun Li [b], Gang-Wang Zhang [a], Tao-Tao Li [c,**]

[a] College of Materials Science and Engineering, Taiyuan University of Technology, Taiyuan 030024, PR China
[b] Taiyuan Iron & Steel Co., Ltd., Taiyuan 030003, PR China
[c] School of Mechanical Engineering, North University of China, Taiyuan 030051, PR China

HIGHLIGHTS

- Prior deformation caused Laves phase to precipitate at temperatures of 950–1050 °C.
- Recrystallised grain size was nearly constant due to the Laves phase pinning effect on grain boundaries.
- Recrystallised texture of {111}⟨112⟩ formed due to the orientated growth associated with Laves phase.
- Lüders deformation related with the Laves transformation of Fe + Nb_2C → Fe_2Nb + [C].

GRAPHICAL ABSTRACT

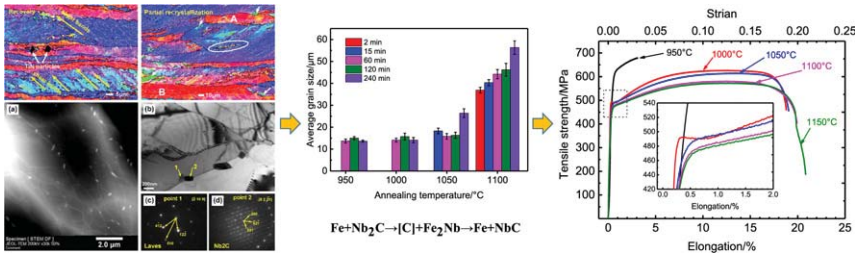

ARTICLE INFO

Article history:
Received 2 October 2019
Received in revised form 7 December 2019
Accepted 4 January 2020
Available online 9 January 2020

Keywords:
Super ferritic stainless steel
Lüders deformation
Annealing
Recrystallization texture
Laves phase
Embrittlement

ABSTRACT

The interaction of microstructural evolution, precipitation and mechanical properties of cold rolled 27Cr–4Mo–2Ni steels stabilised by Nb/Ti during annealing are investigated. Prior deformations provide an acceleration effect on bulk sigma precipitation and increase the starting precipitation temperature to ~1000 °C, which can induce a brittle fracture mode for annealed specimens. The precipitation temperature of Fe_2Nb-type Laves phase is observed to be as high as 1050 °C, and these nanoscale Laves phases are intertwined with Nb_2C particles, which are located at sub-grain boundaries. The abnormal relationship between the grain size and the annealing temperature, which is also related to the formation of Nb-containing particles, is determined. The transformation from Nb_2C to Laves phase below 1050 °C release C atoms into the matrix around the Nb_2C particles. This further leads to Lüders deformation during tensile test because of Cottrell atmosphere formation. The γ-fibre texture development during the annealing process is explained based on orientated nucleation and orientation growth theory. Super ferritic stainless steels exhibit a good combination of strength and ductility via Laves phase precipitation control during annealing at approximately 1050 °C for 5–60 min; these properties are advantageous for their application with strong γ-fibre texture.

1. Introduction

Super ferritic stainless steels (SFSSs), which are originally designed for manufacturing seamless tubes worked with seawater medium, are employed as replacement of copper and titanium pipes because of their high corrosion resistance, good thermal conductivity, small

* Correspondence to: W. Liang, Taiyuan University of Technology, PR China.
* Correspondence to: T.-T. Li, North University of China, PR China.
E-mail addresses: liangwei@tyut.edu.cn (W. Liang), 1317239836@qq.com (T.-T. Li).

https://doi.org/10.1016/j.matdes.2020.108477

coefficient of thermal expansion, and low production cost [1–5]. The pitting resistance equivalent number (PREn = %Cr + 3.3% × Mo) of SFSSs is larger than 35 because 26–32% Cr and 2–4% Mo are added into these alloys. With a low nickel content and a reasonable molybdenum content, SFSSs are proven to be cost effective compared with austenitic and duplex grades [6,7]. The high Cr and Mo concentrations in the structure allow SFSSs to have considerable strengths resulting from their solid–solution hardening [8–10]. These concentrations, however, increase the risk of brittle fracture and corrosion degradation induced by the formation of chromium carbide, such as $Cr_{23}C_6$ or Cr_2N. Ultra-low C and N are therefore preferred for SFSSs [11]. Considering the high cost of extreme purification, carbide/nitride-forming elements, including Nb and Ti, are added to stabilise the residual C and N after moderate purification [12,13]. It is important to improve the processability of the production of thin–walled or other thin-stamped parts using ferritic stainless steels, especially SFSSs. The optimization of parameters for the production process, however, is confronted with problems [7,8,14,15]. There are several factors that limit the processability of SFSSs. First, because of their high Cr and Mo contents, SFSSs maintain a body-centred cubic (BCC) structure until the melting temperature is reached [10,14]. This eliminates the chance of grain refinement by phase transformation, which occurs in carbon steels [16]. Second, several brittle intermetallics, such as (Fe-Cr-Mo)-type sigma (σ), (Fe–Cr–Mo)–type chi (χ) and Fe_2Nb–type Laves (η) phases easily form in the microstructure because of high Cr and Mo contents together with a certain amount of Nb, which is detrimental to toughness and plasticity [8,9,17–22]. Finally, a 475 °C embrittlement also limits the service process of SFSSs [23].

The mechanical properties and various physical properties (yield strength, elongation and stress corrosion cracking resistance) of SFSSs are closely connected with their microstructures (grain size and texture). The control of their microstructure during the production process is therefore crucial to achieve their designed or potential application. Moreover, prior deformation is observed to have a considerable effect on the secondary phase precipitation as well as on the recovery and recrystallisation of their deformed state (structure and texture) [24–26]. On the other hand, the secondary phase particles provide a double-edge influence on both the recrystallisation and mechanical behaviour [27,28]. It is therefore critical to derive the good mechanical properties of SFSSs by the microstructural control and process optimization. Relatively few studies [29–32], however, discuss the interaction effect of Laves phase precipitation, recrystallisation behaviour, and related mechanical properties on SFSSs that contain certain amounts of Nb and Ti.

In this study, the microstructural evolution and mechanical properties of deformed and annealed SFSSs stabilised by Nb and Ti are investigated with the objective of understanding the interaction effect of prior deformation, second-phase precipitation, recrystallisation, and mechanical properties during the production process.

2. Experimental procedures

A continuous cast 27Cr–4Mo–2Ni 200 mm thick super ferritic stainless-steel slab is employed for this investigation; its chemical components are listed in Table 1. The as-received slabs were initially hot-rolled to a t 4.2 mm thickness at a temperature range of 1150–980 °C. These hot-rolled slabs are first solution-treated at 1100 °C for 20 min, followed by water quenching. Second, a cold- rolling experiment is performed with a total reduction of 60%, 70% and 80%. Finally, the cold rolled sheets are annealed at a temperature of 600–1150 °C for 2–240 min followed by water quenching.

A Tescan Mira 3 field emission scanning electron microscope (FE-SEM) equipped with both backscattered electron and electron back scattering diffraction (EBSD) is employed to characterise the microstructure morphology of the longitudinal section (normal direction (ND) and rolling direction (RD)) of the specimens, which are mechanically polished and thereafter electrochemically polished at −30 °C using a perchloric acid alcohol solution at 25 V for 0.5–1.0 min. In the EBSD measurement, the scan steps are set as 0.2–2.5 μm according to the initial grain sizes. The recrystallisation fraction is calculated using Channel 5 software based on the EBSD data. The recrystallisation grains were defined with the critical misorientaion for grain and sub-grain boundaries of 15° and 5°, respectively. The texture is displayed by using the ODF (orientation distribution function).

Transmission electron microscopy (TEM) JEOL 2100F is employed to further show the detailed microstructure of specimens by selected area electron diffraction (SAED) high-angle annular dark field (STEM-HAADF) imaging and high-resolution TEM. The thin foil specimens are produced by double electrolytic jet processing.

Room temperature tensile experiments are performed on an electronic material testing machine (CMT5250) at a rate of 0.5 mm/min controlled by an extensometer. Sub-size specimens with a gauge section of 25 mm × 6 mm are prepared according to ASTM-E8M. Three equivalent specimens were measured under each condition and the standard deviations of the measured values are also calculated.

3. Results

3.1. Room temperature tensile properties

Fig. 1 shows the engineering stress–strain curves for the 80% cold-rolled sheets after annealing at 950–1150 °C for 60 min. It is evident that a high ultimate tensile strength (UTS, ~679 MPa) and yield strength (0.2% proof stress, YS, ~635 MPa) with an extremely low total elongation (TE, ~3.1%) are measured for sheets annealed at 950 °C. After annealing beyond 1000 °C, the UTS and YS evidently decrease, whereas the corresponding TE increases compared with that at 950 °C. When the annealing temperature is between 1100 and 1150 °C, good tensile properties are obtained. The UTS is 570–580 MPa, YS is 485–495 MPa, and TE is ~20.0%, and the tensile curves for the specimens practically overlap. In particular, a weak Lüders elongation phenomenon [33,34] is observed in the specimens annealed at 1000 °C, as shown in the enlarged view embedded in Fig. 1. The upper yield point appears under the condition where the TE is approximately 0.35% with a stress of ~492.6 MPa, whereas the lower yield point locates at ~0.69% with a stress of ~489.7 MPa. Moreover, the yield point elongation persists from 0.35% to 0.95%. For specimens annealed above 1050 °C, however, Lüders deformation is practically invisible.

3.2. Deformed state

Fig. 2 shows the cold microstructure and the related micro-texture characterised by the EBSD technique. Few regions are poorly indexed (Fig. 2a) because of a large residual stress in the microstructure. A recovery annealing at 600 °C for 1440 min is performed to improve the index quality for texture measurement (recrystallisation fraction is ~3.5%); the orientation distribution function (ODF) is shown in Fig. 2b. The cold-rolling microstructure consists of elongated grains along RD with a width in ND of ~2–10 μm. The grain orientation is characterised by

Table 1
The chemical composition of 27Cr–4Mo–2Ni SFSS (wt%).

C	Si	Mn	P	S	Cr	Ni	Mo	Cu	Nb	Ti	N	Fe
0.015	0.4	0.23	0.022	0.002	27.57	1.98	3.72	0.05	0.37	0.14	0.016	Bal.

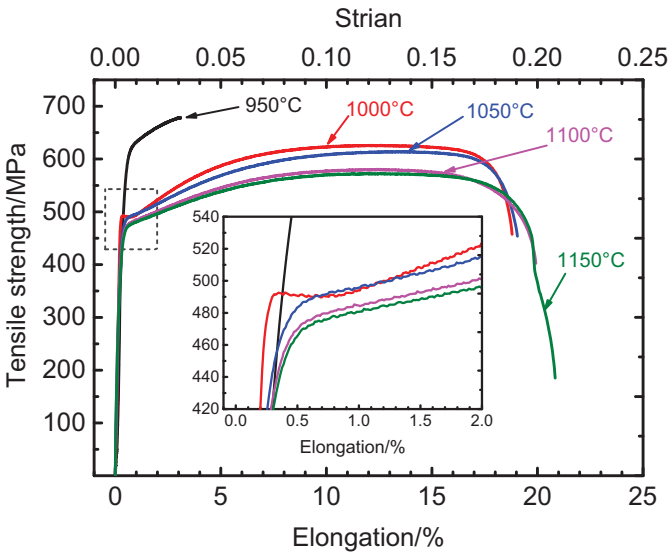

Fig. 1. Engineering stress–strian curves for 80% cold rolled sheets annealed at 950–1150 °C for 60 min.

partial α-fibre (⟨110⟩//RD, running from {001} ⟨110⟩ to {111} ⟨110⟩) and whole γ-fibre (⟨111⟩//ND) texture components (Fig. 2b), which are the representative deformation textures for low carbon steels and ferritic stainless steels [35–37]. Specifically, the α-fibre texture is dominant, and the peak is focused on {112} ⟨110⟩ component because of the large rolling reduction (80%) during cold rolling [36]. Moreover, both intra-granular and inter-granular deformation inhomogeneities are observed. For example, region A (red region presents practically θ-orientated grains) shows a larger deformation than region B, and regions A and B exhibit more uniform deformations than region C (blue region presents practically γ-orientated grains), as shown in Fig. 2a. The elongated grains in region A are 2–5 μm wide along ND, whereas the deformed grains in region B are 5–10 μm wide. A number of shear bands are observed in the γ-orientated grains with a deflection angle of ~17–35° along RD (marked with white arrows in Fig. 2a). In addition, some {110} ⟨001⟩-orientated sub-structures (green region) are also observed within the shear bands.

3.3. Recovery and recrystallisation

Fig. 3 shows the representative recovery and part recrystallisation microstructures of specimens annealed at 600 °C with an 80% reduction. After annealing for 30 min, the recovery is activated in the most heavily deformed regions. A typical local area with a heavy deformation is shown in Fig. 3a. Few banded structures consisting of numerous 1–5-μm sub-grains are found aligned at ~35° to the RD (marked with yellow lines in Fig. 3a). These banded structures are evidently developed along the shear bands, as shown in Fig. 3a. Furthermore, the sub-grains are orientated around the Goss orientation ({110} ⟨100⟩) and γ-fibre, which is considered as the nuclei site for recrystallisation nucleation in ferrous alloys [38]. In particular, high-strain regions around TiN particles that contain a number of LAGB (low-angle grain boundary with a misorientation of 2–15°) are also observed in the microstructure. As the annealing time increases to 2880 min, the combined microstructure of recovery and recrystallisation is observed, as shown in Fig. 3b. Several recrystallised grains, 5–10 μm in size, are found to be embedded in the γ-orientated regions, which have evolved from the sub-grains along the shear bands (marked by yellow arrows in Fig. 3b). On the other hand, the ⟨001⟩//ND regions (A and B in Fig. 3b) remain unrecrystallised or in the recovered state with several LAGBs in these grains.

Fig. 4a shows the recrystallisation kinetic annealing at 950–1100 °C. It is evident that full recrystallisation (definition: recrystallisation fraction ≥95%) is rapidly completed in 2 min when the annealing temperature is >1000 °C. >240 min is required for specimens annealed at 1000 °C. During the annealing treatment at 950 °C, full recrystallisation seems abnormally difficult to accomplish even if the annealing time reaches 240 min. The recrystallisation fraction increases from ~79.8% to 88.0% when the annealing time is prolonged from 2 to 60 min, whereas it anomalously decreases to ~60.5% when the annealing time is further extended to 240 min (Fig. 4a).

The average grain size distribution measured by the EBSD shown in Fig. 4b indicates that the size increases as the annealing temperature increases. On the other hand, the grain size scarcely changes in spite of

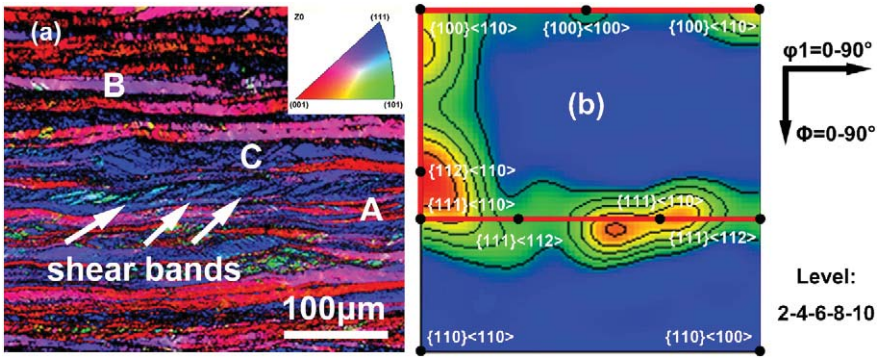

Fig. 2. Microstructure and micro-texture of 80% cold rolled: (a) IPF-Z and (b) constant φ2 = 45°orientation distribution function (ODF).

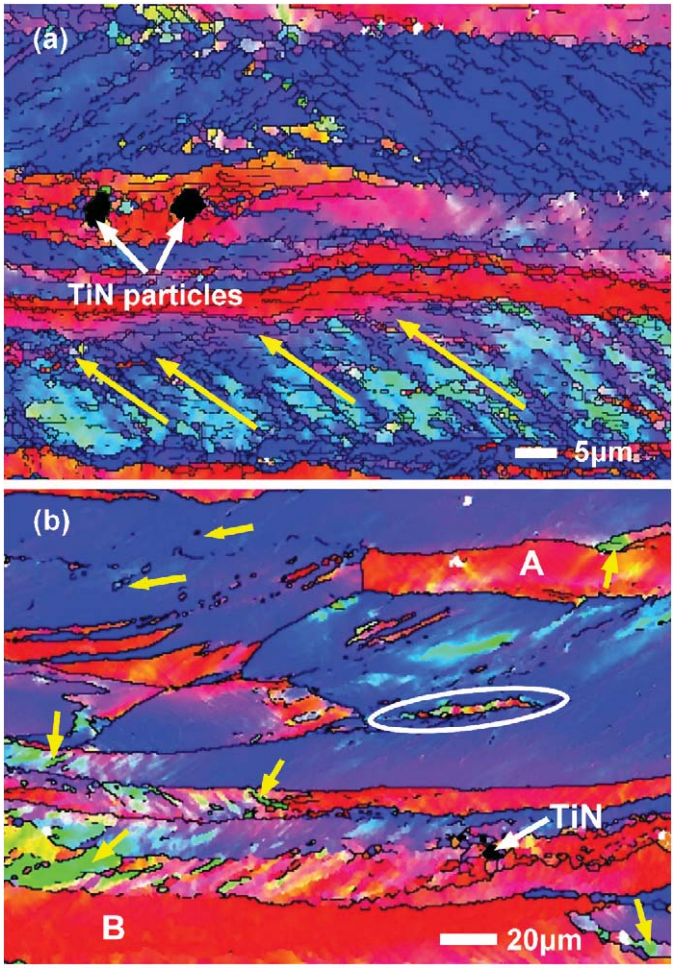

Fig. 3. IPF-Z maps of 80% cold rolled specimens annealed at 600 °C for (a) 30 min and (b) 48 h. The color orientation triangle is same as that in Fig. 2a. The black lines represents the boundaries with misorientaion >5° in (a) and >15° in (b).

increasing the annealing time from 2 to 240 min when the heating temperature is <1050 °C. The sizes also reduce in the range ~13–16 μm, which deviates from the traditional understanding that the grain size increases continuously with increasing temperature and time [8,9,15]. At an annealing temperature of 1050 °C, a visible grain growth (~26.4 μm) is observed only when the annealing time is ≥240 min. The grain size significantly increases with increasing annealing time at 1100 °C, and the maximum grain size of ~59.2 μm is reached after annealing for 240 min.

Fig. 5 shows the recrystallised microstructure and related microtexture evolution after annealing at various temperatures for 60 min. After annealing at temperatures <1000 °C, few elongated grains along the RD together with several fine recrystallised grains (<5 μm) are found in the microstructure. This indicates the occurrence of an incomplete recrystallisation with a fraction of ~22.3% at 950 °C. These unrecrystallised grains are characterised by an approximate θ orientation, and a large number of LAGBs (marked by white lines in Fig. 4) are measured with frequencies of ~23.9% and 17.4% at 950 and 1000 °C, respectively, especially in the elongated grains. When the annealing temperature is >1050 °C, the microstructure consists of fully equiaxed grains with an LAGB of 10.2% at 1100 °C. The constant φ2 = 45° ODF, which is calculated using Channel 5 software, is embedded in the corresponding inverse pole figure. As the temperature increases, the texture gradually progresses from the α-fibre texture towards the γ-fibre texture component (mainly {111}⟨112⟩), which is reported to be beneficial for the formability of FSS [39,40]. Furthermore, the maximum texture intensity is enhanced from 7.36 (at {112}⟨110⟩ for 950 °C) to 11.1 (at {111}⟨112⟩ for 1100 °C).

3.4. Precipitation

Fig. 6 shows the representative morphology of the intermetallic phase after annealing at 950–1100 °C for 60 min. After annealing at 950 °C for 60 min, the bulk sigma phase, nano-size Laves phase, and Nb_2C, as well as TiN and Nb(C, N) particles, are observed in the microstructure. The sigma phase is formed at both grain boundaries and shear bands, as well as around TiN particles, because of the high energy stored in these regions (Fig. 6a) [41]. In particular, numerous microcracks are found within the bulk sigma phase (inset in Fig. 6a) because of the fast precipitation kinetics and the brittle nature of this phase [9]. The sigma phase is well indexed by the EBSD, and the interface between the sigma phase and ferrite matrix belongs to the relationship of {202}σ//{110}α with the deviation peak at ~12.3° (Fig. 7). The fine Laves phase (200–500 nm) also nucleates at the grain and subgrain boundaries (Fig. 6a). The formation of TiN and Nb(C, N) particles are the result of stabilisation reactions during the solidification process because of their high reaction temperature (analysed in our previous study based on thermodynamic calculations and experimental observations [8,9,14]). After annealing at 1000 °C for 60 min, few sigma-phase precipitations, ~3.9 ± 0.3%, are detected compared with those (~9.7 ± 0.7%) at the 950-°C annealing. Numerous Fe_2Nb-type Laves phase and Nb_2C particles, however, are observed at the sub-grain/grain boundaries except for the previously mentioned TiN and Nb(C, N) particles, as shown in the TEM image in Fig. 8. As the annealing temperature further increases to 1050 °C, no sigma-phase precipitation appears, whereas both Laves phase and Nb_2C particles are found; the total Laves phase and Nb_2C volume fraction is 0.22 ± 0.02%. When the annealing temperature reaches 1100 °C, only TiN and Nb(C, N) or NbC particles are observed. The results of further EDS (energy dispersive spectrum) analysis summarised in Table 2 indicate that the sigma phase mainly consists of Fe, Cr, and Mo, whereas the Laves phase is enriched with Nb and Mo elements, which are approximately $(Fe, Cr, Ni)_2$ (Mo, Nb, Si)-type Laves phase.

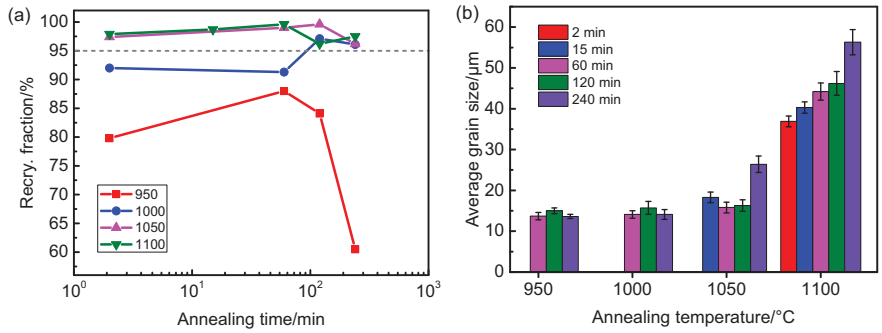

Fig. 4. The recrystallization kinetics and the average grain size distribution of the 80% cold rolled specimens after 950–1100 °C annealing for various time.

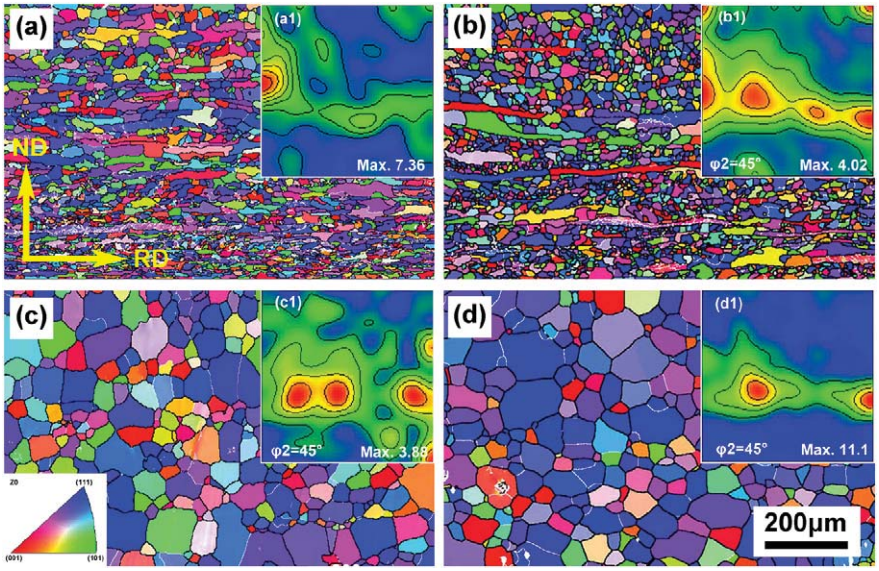

Fig. 5. IPF-Z images for 80% cold rolled sheets after annealing at 950–1100 °C for 60 min: (a) 950 °C, (b)1000 °C, (c)1050 °C and (d) 1100 °C. The a1, b1, c1 and d1 are the corresponding constant $\varphi 2 = 45°$orientation distribution function (ODF) calculated using Channel 5 software. (The white lines represents the LAGB with the misorientaion of 2–15° and the high-angle grain boundary (HAGB) with the misorientaion above 15° are marked by blank lines).

4. Discussion

4.1. Recrystallised texture evolution during annealing

The texture phenomenon usually occurs during the deformation and subsequent annealing of ferrous alloys, such as interstitial free steels [42], electrical steels [43], and ferritic stainless steels [36,44]. The formation of texture may be related to their properties, such as formability and magnetic property; hence, microstructure control is important to ferrous alloys [42–44].

Orientation dependence is usually represented by the Taylor factor, M, which is described as follows [45–47]:

$$M = \frac{\sigma_{ij}}{\tau_c} = \frac{\Sigma\delta_{\gamma k}}{\delta\varepsilon_{ij}} \tag{1}$$

where $\delta_{\varepsilon ij}$ is the plastic strain increment in a state of stress, σ_{ij}; τ_c is the critical resolved shear stress; $\Sigma\delta_{\gamma k}$ is the sum of shear strain on a given slip system to achieve the strain, $\delta_{\varepsilon ij}$. The M value map for the rolling deformation with $\varphi_2 = 45°$ ODF was separately calculated by Sun [29] and

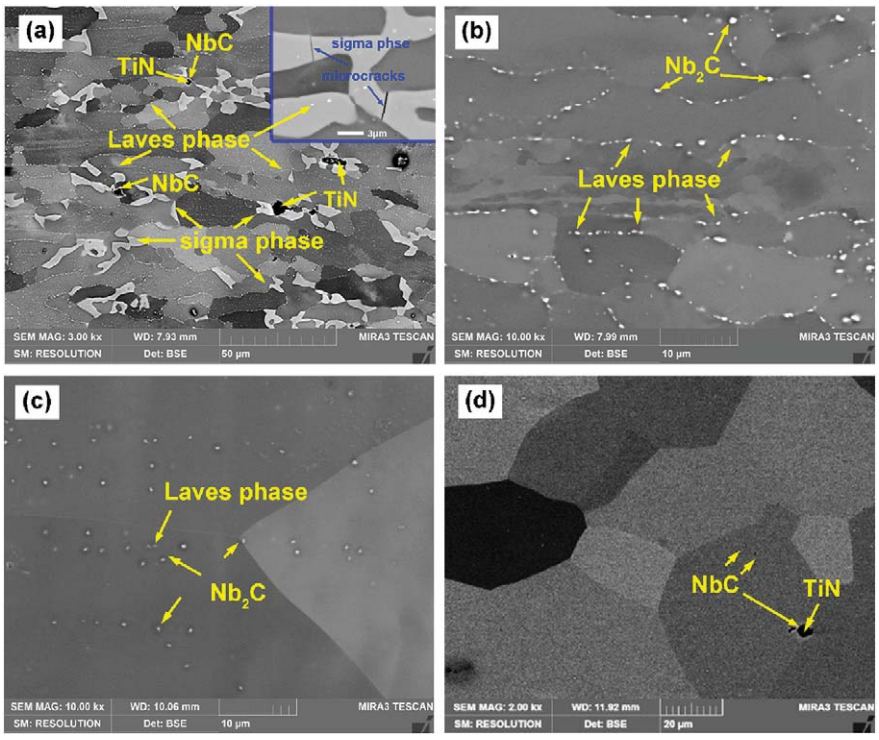

Fig. 6. SEM-BSE morphology of intermetallics for 80% cold rolled sheets after annealing at 950–1100 °C for 60 min: (a) 950 °C, (b)1000 °C, (c)1050 °C and 1100 °C.

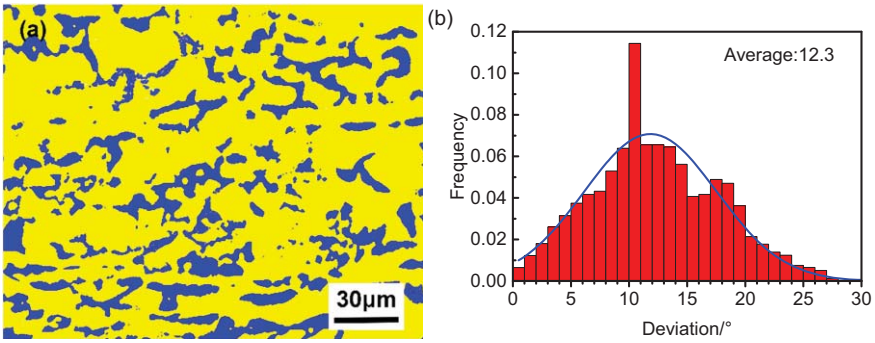

Fig. 7. (a) Sigma phase distribution and (b) the related phase interface deviation meaasured by EBSD in 80% cold rolled specimens after 950 °C annealing for 240 min (in image (a), the yellow regions represent the ferrite, and the bule regions represent the sigma phase).

Kestens [37]. The results reported by Sun are displayed in Fig. 9. According to the calculated results, the θ-fibre texture possesses a small *M* value of ~2.5, whereas the γ-fibre texture has a larger *M* value of 3.7 (at {111}⟨112⟩) and 4.1 (at {111}⟨110⟩). The *M* values of α-fibre texture range from 2.5 to 4.1, which correspond to the texture component shifting from {001} ⟨110⟩ to {111} ⟨110⟩ along α orientation lines. Eq. (1) also shows that large *M* values indicate a shear strain on a given applied strain. During the plastic deformation, the stored strain energy, *E*, is also orientation-dependent with the sequence $E_{110}>E_{111}>E_{112}>E_{100}$ (relative to the ND) [48,49].

In this study, typical deformed α-fibre (from {001} ⟨110⟩ to {111} ⟨110⟩) and γ-fibre textures are formed because of the small *M* values of α and γ-orientated grains. The *M* values of α-fibre texture that are smaller than those of γ-fibre texture create a more uniform deformation in the interior of α-orientated grains than that in γ-orientated grains. Moreover, the large *M* values of γ-fibre texture also cause the formation of shear bands in these grains. When the largest *M* values are in the ⟨110⟩//ND texture, some ⟨110⟩-orientated substructures are observed within the shear bands in γ-orientated grains.

After recovery annealing, such as at 600 °C, the texture component is practically stable because only dislocation slip and climb, and polygonisation occur [29]. As the annealing temperature or annealing time increases, recrystallisation nucleation is activated. The {110} ⟨001⟩ nuclei preferentially appears within the shear bands in γ-orientated grains because of the initial formation of the {110} ⟨001⟩ structure within the shear bands during cold rolling. This phenomenon is in accord with that in Fe—Si alloys [50,51]. In addition, γ-orientated nuclei ({111}⟨112⟩ and {111}⟨110⟩) are also formed in the considerably deformed γ-orientated grains because of stored high energy and large heterogeneity in these grains according to the oriented nucleation theory [52].

During the recrystallisation annealing at low temperature, i.e., 950 and 1000 °C, the recovery is swiftly activated before the recrystallisation process, and only ⟨110⟩//ND and γ-orientated nuclei develop into recrystallised grains because of stored high-deformation energy. Uniform γ-fibre textures, including {111} ⟨110⟩, {111} ⟨112⟩, and {110} ⟨001⟩, are measured. Moreover, the fast recovery of {112}⟨110⟩ deformed grains also accounts for the remaining elongated grains. Some un-recrystallised grains are retained because of the small residual driving force for recrystallised grain boundary migration. For high-temperature annealing, such as at 1050 and 1100 °C, the {111} ⟨112⟩ grains rapidly develop at the expense of {112} ⟨110⟩ and {111} ⟨110⟩ grains according to the oriented growth theory. For example, there is a 35°⟨110⟩ rotational relationship between the {111} (112) texture and strong cold-rolling texture component of {112} ⟨110⟩ that approaches the ideal 27° ⟨110⟩ rotational relationship, which is characterised by a Σ19a coincidence site lattice. The rotational relationship between {111} ⟨110⟩ and {111} ⟨112⟩ is 30° ⟨111⟩, which approximates the 27.8°⟨111⟩ relationship, specifically the Σ13b coincidence site lattice. The {111} ⟨112⟩ nuclei can selectively grow into the {112} ⟨110⟩ and {111} ⟨110⟩ deformed grains because of the high mobility of these special boundaries (Σ19a and Σ13b). Most {112} ⟨110⟩ and {111} ⟨110⟩ deformed grains are thus exhausted after the annealing treatment, and the recrystallised texture is focused on {111} ⟨112⟩. The stability of Goss texture is maintained when the annealing temperature is <1050 °C because of the initial nucleation position. As the annealing temperature increases to 1100 °C, the Goss texture shifts to {111} ⟨112⟩ because of the rotation of 35°⟨110⟩ between {110} ⟨001⟩ and {111} ⟨112⟩.

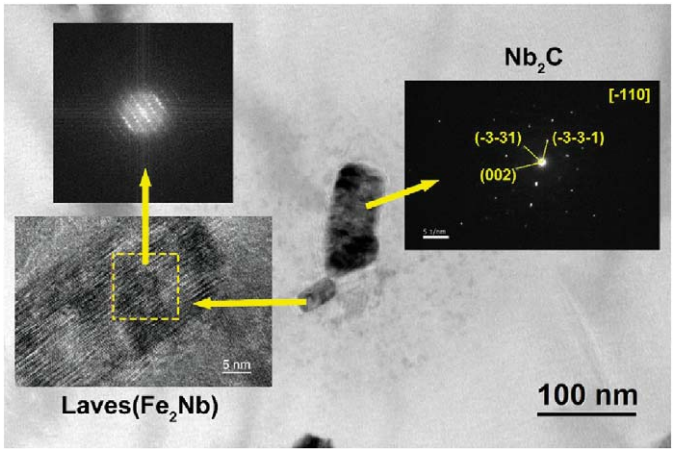

Fig. 8. TEM-BF and HRTEM (high resolution) images showing the Laves transformation from Nb_2C in the 80% cold rolled sheet after annealing at 1000 °C for 2 min.

4.2. Prior deformation effects on precipitation and recrystallisation kinetics

According to previous studies, the sigma phase is usually formed in the temperature range 704–927 °C. On the other hand, the Laves phase for SFSSs, such as 25Cr–3Mo–4Ni [17], 29Cr–4Mo–2Ni [6], 28Cr–4Mo-2Ni [3,4], and 27Cr–4Mo–2Ni [14,15], is formed in the temperature range 650–800 °C after solution treatment. In this research, the tested steels are cold-rolled before the annealing treatment, and the precipitation of sigma and Laves are detected at higher temperatures (>950 °C). The prior cold deformation may therefore have a considerable influence on the sigma-phase formation.

In order to demonstrate the dependence of sigma precipitation on prior cold deformation and annealing conditions, cold-rolled sheets with total reductions of 60%, 70%, and 80% are further analysed using BSE images; results are shown in Fig. 10a. It is evident that the sigma precipitation is accelerated by the increase in cold-rolling reduction both at 950 and 1000 °C annealing. A sigma-phase content of approximately 6.3 ± 0.6% is measured in cold-rolled specimens with a 60% reduction after annealing at 950 °C for 60 min, and 7.5 ± 1.2% and 9.7 ± 0.7% sigma-phase contents are observed in annealed specimens with

Table 2
SEM-EDS results of typical precipitates in annealed 27Cr–4Mo–2Ni SFSS (At.%).

Elements	Fe	Cr	Mo	Nb	Si	Ni
Sigma phase	62.2 ± 1.8	31.3 ± 1.7	5.2 ± 0.8	–	0.4 ± 0.1	1.6 ± 0.3
Laves phase	54.5 ± 3.5	22.0 ± 2.8	8.5 ± 0.9	9.5 ± 1.4	3.8 ± 0.7	1.7 ± 0.4

70% and 80% reductions, respectively. Additionally, sigma precipitation kinetics are compared with recrystallisation kinetics, as shown in Fig. 10b. Visible incubation periods are observed in the sigma precipitation curves for both 950 and 1000 °C annealed specimens. Precipitation kinetics is considerably enhanced as the annealing time increases. The specimens annealed at 950 °C exhibit stronger kinetics than those annealed at 1000 °C. After annealing at 950 °C for 240 min, the maximum sigma-phase content reaches 31.6 ± 2.7%. The kinetics curves in Fig. 10b also indicate that recrystallisation kinetics is faster than sigma-phase precipitation. In general, the secondary phase usually nucleates at the grain boundary, sub-grain boundary, and dislocations [53]. During the preheating process, static recovery and recrystallisation are rapidly activated because of heavy cold rolling (Fig. 3). Moreover, numerous fine recrystallisation grains (the smaller the grain size, the more grain boundaries) and few LAGBs are obtained (Fig. 5). More nucleation sites, such as grain boundaries, dislocations, and regions around TiN particles (several LAGBs are found around TiN particles, as shown in Fig. 3a) are afforded for sigma precipitation (Fig. 6a). The dislocations also provide a fast diffusion route for solutes (such as Cr and Mo) that is necessary for sigma-phase coarsening. The higher amount of energy stored in the deformed microstructure provides a strong driving force for sigma-phase transformation; a similar phenomenon is also observed in the hot rolling and aging process of SFSS [41]. The sigma precipitation temperature reaches higher values, such as 950 and 1000 °C, because the sigma precipitation kinetics is distinctly enhanced by heavy cold-rolling deformations, as shown in Fig. 6.

At an annealing temperature of 950 °C, the recrystallisation fraction first increases then decreases with increasing annealing time (Fig. 4a). This phenomenon is related to the sigma and Laves phase precipitations. For short-time annealing, the recrystallisation nucleation is first activated because the incubation period for recrystallisation is shorter than that for sigma precipitation. As the annealing time increases, the Laves phase content increases and Laves phase particles are found at dislocations. Laves phase particles exhibit a pinning effect on sub-grain and grain boundary migrations. The recrystallisation is thus impeded, and the grains are kept at an elongated state. Moreover, the sigma phase shows fast precipitation kinetics at 950 °C and is characterised by a bulk shape. The fast sigma precipitation and coarsening yield a certain stress to the surrounding ferrite matrix and induce several dislocations in the matrix near the precipitation location. In our previous study, the foregoing phenomenon was also observed [9]. When the sigma precipitation content is sufficiently large, the micro-strains are generated in the matrix, and LAGB is formed. The un-recrystallisation region is thus increased, indicating that the recrystallisation fraction decreased.

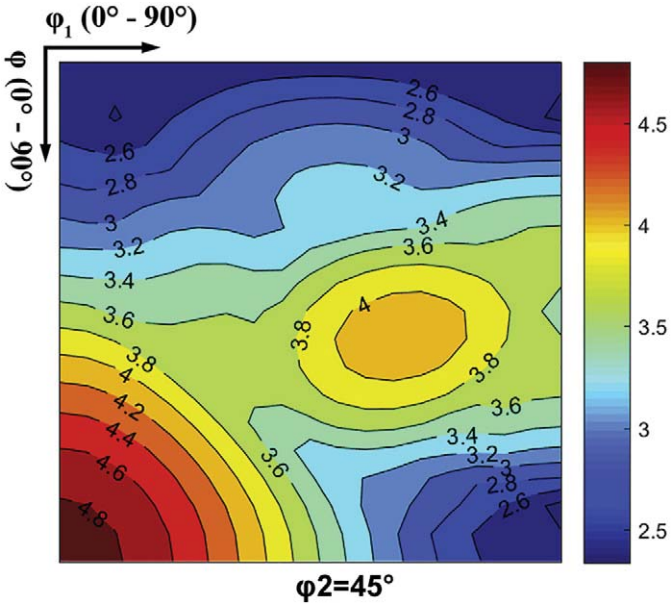

Fig. 9. The calculated Talor factor (M) associating to the $\varphi_2 = 45°$ ODF [29].

4.3. High Laves precipitation induced by prior deformation

In order to evaluate the high-temperature precipitation of Laves phase, TEM analysis is further performed; results are shown in Fig. 11. Numerous intermetallic particles are observed at both sub-grain and grain boundaries in specimens annealed at 1000 °C for 60 min, as shown in the STEM-HAADF image (Fig. 11a). A partially enlarged TEM-BF drawing of the intermetallics in Fig. 11a is also shown in Fig. 11b, and the related SAED of points 1 and 2 in Fig. 11b are displayed in Figs. 11c and 9d, respectively. The SAED results confirm that the Laves phase and Nb_2C particles are interlocked at grain boundaries or sub-grain boundaries. The bright linellae along the boundaries (Fig. 11a) also indicate that the segregations around sub-grain and grain boundaries of atoms, such as Nb, Mo, and Cr, occur because of their high concentrations in steel and high reheating temperature for annealing [54]. The TEM–EDS point analysis is performed around these regions, marked by points 3–7 in Fig. 11a; results are summarised in Table 3. It is evident that high concentrations of Nb and Mo are enriched near the boundaries, and a certain concentration gradient appears from the in-grain to the boundaries. In addition, the thermodynamic calculation under the 1100 °C quenching condition followed by the 1000-°C isothermal aging is also performed using JMat Pro V7; related results are shown in Fig. 12. The calculated results also indicate that both Laves phase and Nb_2C particles are formed during the 1000-°C annealing. V. Kuzucu et al. [55] reported that when ~3.0 wt% Nb is added to 18% Cr ferritic stainless steels, Nb_2C particles are observed to dissolve after annealing at 1100 °C. In this study, several sub-grain boundaries (Fig. 5) are formed by the dislocation climb and cross-slip, i.e., the recovery process during reheating after heavy cold-rolling. Numerous dislocations provide a preferential route for Nb/Mo diffusion; thus, the boundary segregation of Nb and Mo atoms is observed. As the Nb/Mo diffusion continues, the level of Nb at the boundaries satisfies the requirements for Nb_2C and Laves phase formation. The Nb_2C carbides and Laves phase occur during annealing at 1000 °C. When annealing is conducted at 1100 °C, no Nb_2C carbides are found, which is in accord with the report of V. Kuzucu.

4.4. Laves phase precipitation effect on recrystallisation grain size

The recrystallisation grain size is generally controlled by recrystallisation nucleation and grain growth, which are considerably affected by the pinning effect of secondary phases containing Nb, such as Laves phase and Nb_2C located at the sub-grain and grain boundaries.

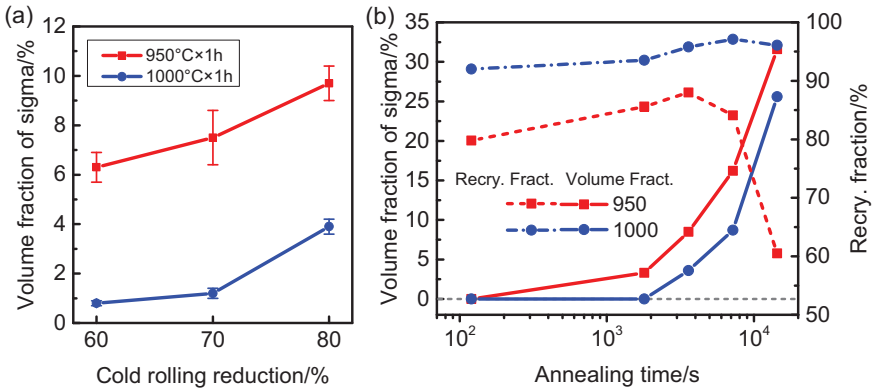

Fig. 10. (a) Effect of cold rolled reduction on the sigma precipitaion and (b) sigma precipitaion kinetics for 80% cold rolled sheets.

The Zener pinning forces by the Nb-containing phase, Pz, can be expressed as [56].

$$P_Z = \frac{3\gamma f l}{2\pi r^2} \tag{2}$$

where γ is the interfacial energy per unit area of boundary; f is the volume fraction of particle; r is the average particle radius; l is the average grain intercept length. The value of l can be related to the average grain diameter, D, by $l = \pi D/4$ [57].

The driving pressure for the recrystallisation-front migration, P_r, can be related to the dislocation density difference ($\Delta\rho$) between recrystallised and non-recrystallised regions by [56,58].

$$P_r = Gb^2\Delta\rho/2 \tag{3}$$

where G is the shear modulus (~50 GPa at 1000 °C); b is Burgers vector length (~0.25 nm); $\Delta\rho$ is estimated to be ~$2.8 \times 10^{14}/m^2$ based on the strain hardening model. Assuming that the average Taylor is 3, this model is given by the following [29,59]:

$$\Delta\sigma \sim 3/2Gb\sqrt{\Delta\rho} \tag{4}$$

where $\Delta\sigma$ (~500 MPa) is the yield stress increment between cold-rolled and fully annealed specimens (annealed at 1050 °C for 2 min); G is ~80 GPa at room temperature for stainless steels [60]. By substituting the foregoing in Eqs. (3) and (4), P_r is estimated to be ~0.4 MPa. For the tested steels after annealing for 60 min at 1000 °C, the Nb-containing phase particle size is ~400 nm, f is ~0.02, and D is ~15 μm; γ is reported to be ~1 J/m^2 [61]. By substituting all parameters into Eq. (3), P_z is determined to be ~0.7 MPa, which is higher than the value of P_r. The recrystallisation is therefore not completed with the ~91% fraction in specimens annealed at 1000 °C for 60 min. Some non-recrystallised regions, however, are still observed because of the reduction in dislocation density induced by the fast recovery process before recrystallisation. As the annealing time increases, the recrystallisation fraction gradually increases because of the slight reduction in the quantity of Nb-containing particles and the rapid recrystallisation nucleation. When annealing is implemented at 1050 °C for 60 min, P_z is ~0.3 MPa because the particles in the microstructure are few (f is ~0.002 and r is ~200 nm), and P_r is ~0.4 MPa. Full recrystallisation is thus facilely completed (Fig. 2a).

For the recrystallised grain growth, the driving pressure, P_g, can be described as [58] follows:

$$P_g = 2\gamma/D \tag{5}$$

where P_g is ~0.14 MPa in the case of annealing at 1000 °C. This pressure is considerably smaller than the P_z value of ~0.7 MPa. Grain growth is therefore difficult to initiate. After annealing at 1050 °C for 240 min, the Nb-containing particles coarsened with a size (r) of ~6 μm, and the volume fraction (f) is approximately 0.0059; thus, P_z is approximately 0.002 MPa, indicating the near-miss of Zener pinning effect. As a result, grain growth is initiated. When the temperature increases to 1100 °C, no Laves and Nb_2C particles are found, and normal grain growth occurs.

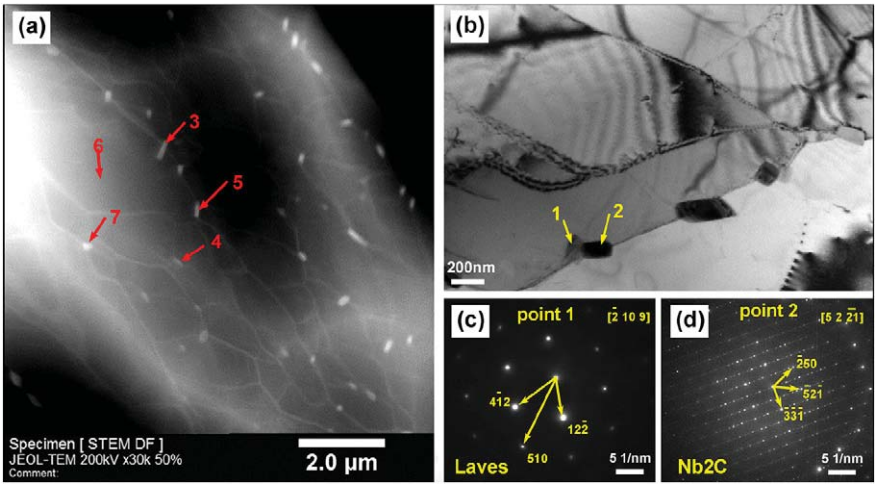

Fig. 11. Precipitaion in 80% cold rolled sheets after annealing at 1000 °C for 60 min: (a) STEM-HAADF; (b) partial enlarged detail with TEM-BF for (a); (c) and (d) are the SAED of point 1 and 2 in (b).

Table 3
Chemical component of measured point in Fig. 7a by TEM-EDS (wt%).

	Fe	Cr	Si	Nb	Mo	Ni
Point 3	54.5	22.0	4.3	9.2	8.3	1.7
Point 4	58.9	28.8	1.4	3.5	4.2	1.7
Point 5	56.1	28.1	1.9	8.3	4.1	1.5
Point 6	62.5	32.9	0.8	–	2.2	1.6
Point 7	58.1	27.0	2.5	5.3	5.5	1.6

4.5. Sigma precipitation embrittlement

The fracture morphology of annealed specimens is shown in Fig. 13. An evident brittle fracture region is observed in specimens with 70%–80% reductions and annealed at 950 °C for 60 min. For specimens annealed at 1000 °C for 60 min, the fracture morphology is mainly composed of dimples. In comparing specimens with various reductions annealed at the same temperature, it is evident that the brittle fracture morphology feature becomes distinct as the amount of reduction is increased from 60% to 80%. This phenomenon indicates that the ductile-to-brittle transition (DBT) occurs when the amount of precipitated sigma phase is abundant. The nano-size Laves phase, however, seemingly exhibits an insignificant influence on toughness, differing from that observed in austenitic stainless steels [62,63]. According to the Cottrell model [64], the DBT occurs when

$$\sigma_y k_y d^{1/2} = k_y^2 + \sigma_0 k_y d^{1/2} > C\mu\gamma \tag{6}$$

where σ_y is the brittle fracture stress or flow stress; k_y is the Hall–Petch slope; d is the average grain size; σ_0 is the lattice friction stress; μ is the shear modulus; γ is the effective surface energy of an implied crack; and C is a constant.

In this study, the value of d is practically constant in the given temperature range, whereas σ_y increases in the course of sigma-phase precipitation. Moreover, the incoherent interface between the sigma phase and ferrite matrix adversely affects their deformation coordination. The foregoing also considerably impedes the slip propagation across grain boundaries that can further increase k_y. This is particularly the case in a continuous grain boundary network resulting from sigma-phase formation. The microcracks within the sigma phase can also act as crack initiation sites and can decrease γ [65]. Furthermore, our previous study [9,41] has shown that sigma phase has a considerably higher Vickers hardness than ferrite matrix, which exhibits a different deformability under tension. As a result, the combination of existing microcracks with the sigma phase, high Vickers hardness, and incoherent interface is the main reason of sigma precipitation embrittlement after high-temperature annealing. The annealing microstructure at 950 °C also exhibits large work hardening (low recrystallisation fraction), which increases k_y. The ductility of specimens annealed at 950 °C is thus further decreased although the sigma precipitation content in the microstructure is only 6%.

4.6. Lüders deformation associated with Laves transformation

Ferritic stainless steels are usually machined by the forming process, during which the homogeneous plastic deformation is required [44]. In this study, Lüders deformation is determined for specimens annealed at 1000 °C, which is undesired for the aforementioned alloy. Compared with the microstructure of specimens annealed at other temperatures, Laves phase precipitation has the most remarkable difference, and Lüders deformation is considered to be related to Laves phase transformation.

For ferritic stainless steels, the solubility product of Laves phase (in mass %) can be described as follows [66].

$$\log[\mathrm{Nb}] = \frac{-3780.3}{T} + 2.4646 \tag{7}$$

The soluble contents of [Nb] at 1050, 1000, and 950 °C are approximately 0.40%, 0.31%, and 0.25%, respectively. In the tested steels, approximately 0.37% Nb is added into the alloy. If all [C] is formed as NbC, 0.12% Nb would be consumed. If [C] is formed as Nb_2C, 0.23% Nb is required. In this study, the microstructure of two types of niobium carbide, NbC and Nb_2C, is formed. The required Nb for stabilising [C] is thus 0.12%–0.23%, which leaves 0.14–0.25% Nb for the formation of Fe_2Nb. According to Eq. (7), the residual Nb content is smaller than the solubility in the temperature range 1000–1050 °C. The Nb content is therefore insufficient for the formation of Fe_2Nb in the specimens annealed at 1000–1050 °C. As a result, high-temperature Laves precipitation is seemingly not driven by the decrease in the solubility product of Nb that is applicative to low-temperature Laves precipitation [65].

A study of V. Kuzucu [55] shows that Nb_2C particles facilely form in ferritic stainless steels when Nb is up to 3.0%. With increasing annealing temperature, these Nb_2C particles transform into NbC. In this study, the boundary segregation of solute atoms (Nb) occurs because of numerous LAGBs or sub-grain boundaries in the microstructure that are induced by static recovery after heavy cold-rolling (Fig. 11a). The Nb concentration that accumulates in these local positions around the boundaries is considerably higher than 3.0% (Table 3); accordingly, Nb_2C particles

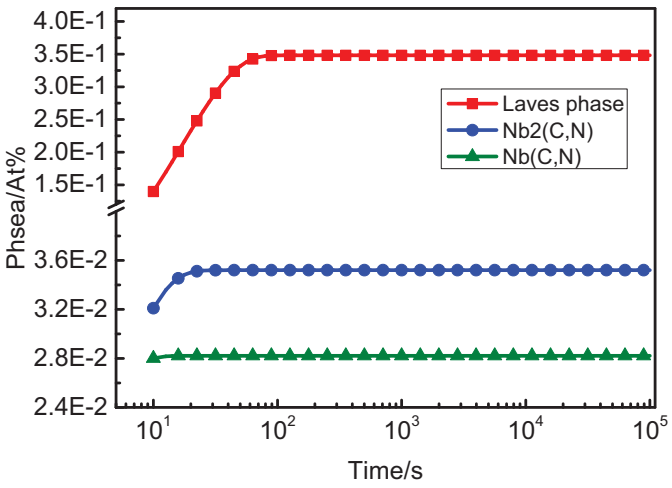

Fig. 12. Calculated precipitaion evolution of Laves phase, $Nb_2(C,N)$ and Nb(C,N) particles in the tested specimens held at 1000 °C after 1100 °C solution treating.

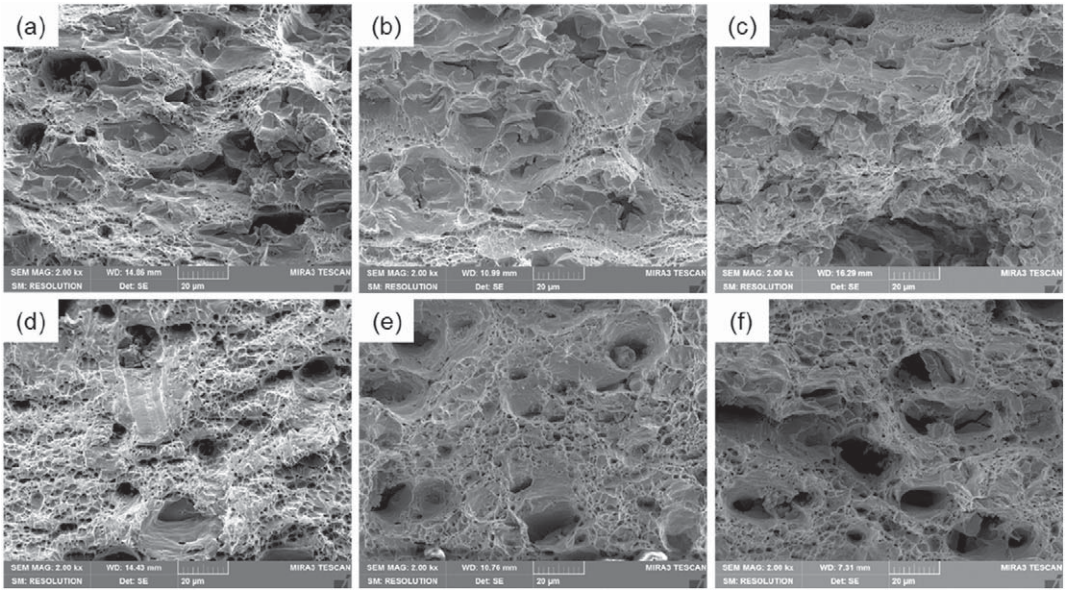

Fig. 13. The fracture morphology of sheets annealed at (a–c) 950 °C for 60 min and (d–f)1000 °C for 60 min with (a, d) 60%, (b, e) 70% and (c, f) 80% rolling reductions.

are formed. As the annealing temperature (such as 1000 °C) increases, Nb_2C particles are transformed into Fe_2Nb-type Laves phase, and free C atoms are simultaneously released according to the following.

$$Fe + Nb_2C \rightarrow [C] + Fe_2Nb \rightarrow Fe + NbC \quad (8)$$

High-temperature Laves phase precipitation therefore occurs. After the above-mentioned transformation process, [C] atoms are extruded and distributed around the Fe_2Nb phase; the schematic is shown in Fig. 14. In the subsequent tensile test at room temperature, the Cottrell atmosphere [34,67] forms and results in Lüders deformation. When the annealing temperature increases to 1050–1100 °C, the C distribution homogenisation is advanced, and only NbC or Nb(C,N) particles are observed. As a result, Lüders deformation phenomenon does not occur.

In conclusion, induced by prior cold rolling, Laves phase particles form at a high temperature of ~1050 °C. These provide the pinning effect on grain growth for Nb-stabilised SFSSs. Meanwhile, brittle sigma-phase precipitation does not occur. Moreover, apart from the mechanical properties, uniform γ-fibre texture, which improves these properties, is obtained. The pre-precipitation of Laves phase at ~1050 °C is a potential route to achieve an optimum microstructure for Nb-stabilised SFSSs production.

5. Conclusions

A hot-rolled 27Cr–4Mo–2Ni SFSS is cold-rolled and annealed at 950–1100 °C. The microstructural evolution, precipitation, and mechanical properties are investigated. Some of the conclusions drawn are as follows.

1. The cold-rolled deformation texture is composed of α-fibre and γ-fibre. Several shear bands are observed within γ-oriented grains, whereas uniform deformations appear in θ-fibre grains and α-fibre

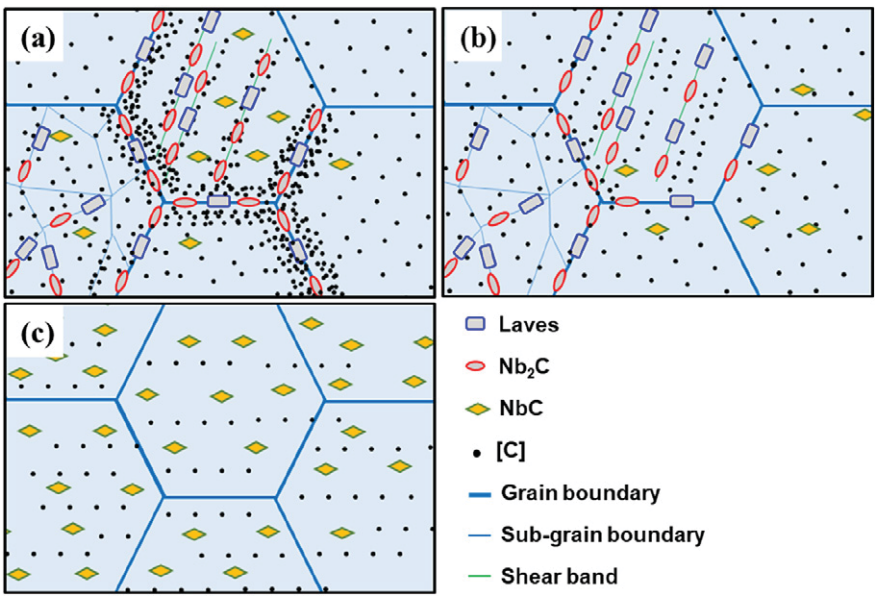

Fig. 14. Schematic diagram for release of C atoms accociated to Laves phase transformation from Nb_2C particles: (a) 1000 °C, (b) 1050 °C and (c) 1100 °C.

grains because of strong deformation heterogeneity. The strong γ-fibre texture is obtained after recrystallisation annealing because of the preferential nucleation at shear bands within heavy deformation grains.

2. Prior deformation accelerates the sigma formation and enhances the starting precipitation temperature to 1000 °C because of the presence of considerably numerous nucleation sites, including grain boundaries, sub-grain boundaries, shear bands, and regions around TiN particles. The sigma precipitation and coarsening decrease the recrystallised kinetics and substantially deteriorate tensile plasticity.
3. Nano-size Nb-containing particles, such as Laves phase and Nb_2C, are formed at grain and sub-grain boundaries after annealing at 950–1050 °C. These particles do not deteriorate the tensile plasticity. When they are dissolved at 1100 °C, only TiN and NbC/N particles remain.
4. The grain growth during recrystallisation is inhibited by the boundary precipitation of Nb-containing particles, including Laves phase and Nb_2C, because of their pinning effect on grain boundary migration.
5. The transformation of Laves phase from Nb_2C releases numerous C atoms into the matrix around these Nb-containing particles. It further results in Lüders deformation during the tensile deformation because of the formation of Cottrell atmosphere.

Author contribution statement

The first author (Hui-Hu Lu) presented the research idea and experimental design, and wrote this manuscript. The second author (Hong-Kui Guo) assisted to complete the cold-rolling and annealing experiment. The fourth author (Jian-Chun Li) helped to carry out the hot-rolling experiment. The fifth author (Wang-Gang Zhang) put forward some instructive suggestions for the writing of this paper and modified the language. The sixth author (Tao-Tao Li) helped to fulfill the work of SEM and EBSD analysis. The TEM analysis was completed by the corresponding author (Wei Liang) and Tao-Tao Li.

Declaration of competing interest

The authors declare that they have no known competing financial interests or personal relationships that could have appeared to influence the work reported in this paper.

Acknowledgements

This work was supported by the Projects of International Cooperation in Shanxi, China (Grant No.: 201603D421026) and the Innovation Project of Shanxi Province Graduate Education (Project title: Laves phase high temperature precipitation behavior and its effects on the recrystallization texture in super-ferritic stainless steel).

Data availability statement

The raw data related to this paper would be made available on request.

References

[1] S. Kumar, R.K. Vijayavergia, S. Chakraborty, Super ferritic stainless steels: an overview, Tool Alloy Steel (1995) 38–396.
[2] D.S.J.A. Henricks, Superferritic stainless steels–the cost effective answer for heat transfer tubing, Stainl. Steel World (2005) 184–190.
[3] Michael A. Streicher, Development of pitting resistant Fe–Cr–Mo alloys, Corrosion 30 (1974) 77–91.
[4] T.J. Nichol, Microstructures and some properties of Fe–28%Cr–4%Mo alloys, Metall. Trans. A. 8 (1974) 115–124.
[5] N. Pessall, J.I. Nurminen, Development of ferritic stainless–steels for use in desalination plants, Corrosion 30 (1974) 381–392.
[6] T.J. Nichol, Mechanical properties of a 29 Pct Cr–4 Pct Mo–2 Pct Ni ferritic stainless steel, Metall. Trans. A. 8 (1977) 229–237.
[7] L. Ma, S.S. Hu, J.Q. Shen, J. Han, Effects of annealing temperature on microstructure, mechanical properties and corrosion resistance of 30% Cr super ferritic stainless steel, Mater. Lett. 184 (2016) 204–207.
[8] H.-H. Lu, H.-K. Guo, L.-Y. Du, Z.-G. Liu, J.-C. Li, W. Liang, Formation of intermetallics and its effect on microstructure and mechanical properties of 27Cr–4Mo–2Ni super ferritic steels, Mater. Charact. 151 (2019) 470–479.
[9] H. Lu, Y. Luo, H. Guo, W. Li, J. Li, W. Liang, Microstructural evolution and mechanical properties of 27Cr–4Mo–2Ni ferritic stainless steel during isothermal aging, Mater. Sci. Eng. A 735 (2018) 31–39.
[10] L. Ma, S. Hu, J. Shen, J. Han, Z. Zhu, Effects of Cr content on the microstructure and properties of 26Cr–3.5Mo–2Ni and 29Cr–3.5Mo–2Nisuper ferritic stainless steels, J. Mater. Sci. Technol. 32 (2016) 552–560.
[11] I.A. Franson, Mechanical properties of high purity Fe–26 Cr–1 Mo ferritic stainless steel, Metall. Trans. A. 5 (1974) 2257–2264.
[12] T. Fukuda, Effect of titanium carbide precipitates on the ductility of 30 mass% chromium ferritic steels, Mater. Trans. 44 (2003) 1153–1158.
[13] K. Premachandra, M.B. Cartie, R.H. Eric, Effect of stabilising elements on formation of σ phase in experimental ferritic stainless steels containing 39%Cr, Mater. Sci. Technol. 8 (2013) 437–442.
[14] H.H. Lu, W.W. Lei, Y. Luo, J.C. Li, Z.G. Liu, W. Liang, Microstructural evolution, precipitation and mechanical properties of 27Cr–4Mo–2Ni super-ferritic stainless steels, JOM (2019) 1–10.
[15] H.P. Qu, Y.P. Lang, H.T. Chen, F. Rong, X.F. Kang, The effect of precipitation on microstructure, mechanic properties and corrosion resistance of two UNS S44660 ferritic stainless steels, Mater. Sci. Eng. A 534 (2012) 436–445.
[16] L. Ma, J. Han, J.Q.S.S. Hu, Acta Metall. Sin. (Engl. Lett.) 27 (2014) 407–415.
[17] E.L. Brown, M.E. Burnett, P.T. Purtscher, G. Krauss, Intermetallic phase formation in 25Cr–3Mo–4Ni ferritic stainless steel, Metall. Trans. A. 14 (1983) 791–800.
[18] S. Saito, N. Tukuno, M. Shimura, E. Tanaka, Y. Katuara, T. Ototani, On the embrittlement and toughness of high purity Fe–30Cr–2Mo alloy. In toughness of ferritic stainless steels, ASTM STP 706 (1980) 77–98.
[19] T.J. Nichol, A. Datta, G. Aggen, Embrittlement of ferritic stainless steels, Metall. Trans. A. 11A (1980) 573–585.
[20] M.K. Veistinen, V.K. Lindroos, Cleavage fracture strength of a 26Cr–lMo ferritic stainless steel, J. Heat Treating 4 (1985) 56–68.
[21] W. Haoquan, W.S. Spear, D.H. Polonis, Influence of annealing and aging treatments on the embrittlement of type 446 ferritic stainless steel, J. Mater. Eng. 9 (1987) 51–61.
[22] T. Yamagishi, M. Akita, M. Nakajima, Y. Uematsu, K. Tokaji, Effect of σ–phase embrittlement on fatigue behaviour in high–chromium ferritic stainless steel, Procedia Eng. 2 (2010) 275–281.
[23] L.B. Moura, H.F.G. de Abreu, W.S. Araújo, J.F.B. Franco, M.C. Sampaio, F.E.R. Maurício, Embrittlement and aging at 475 °C in an experimental superferritic stainless steel with high molybdenum content, Corros. Sci. 137 (2018) 76–82.
[24] Y. Keisuke, K. Yoshisato, M. Yoshinao, Effect of matrix substructures on precipitation of the Laves phase in Fe–Cr–Nb–Ni system, ISIJ Int. 43 (2003) 1253–1259.
[25] Z.-W. Hsiao, D. Chen, J.-C. Kuo, D.-Y. Lin, Effect of prior deformation on microstructural development and Laves phase precipitation in high-chromium stainless steel, J. Microsc. 0 (2017) 1–13.
[26] I. Bikmukhametov, H. Beladi, J. Wang, P.D. Hodgson, I. Timokhina, The effect of strain on interphase precipitation characteristics in a Ti-Mo steel, Acta Mater. 170 (2019) 75–86.
[27] Ke Huang, Knut Marthinsen, Qinglong Zhao, Roland E. Logé, The double-edge effect of second-phase particles on the recrystallization behaviour and associated mechanical properties of metallic materials, Prog. Mater. Sci. 92 (2018) 284–359.
[28] B. Kuhn, M. Talik, L. Niewolak, J. Zurek, H. Hattendorf, P.J. Ennis, W.J. Quadakkers, T. Beck, L. Singheiser, Development of high chromium ferritic steels strengthened by intermetallic phases, Mater. Sci. Eng. A 594 (2014) 372–380.
[29] Z. Sun, P.D. Edmondson, Y. Yamamoto, Effects of Laves phase particles on recovery and recrystallization behaviors of Nb-containing FeCrAl alloys, Acta Mater. 144 (2018) 716–727.
[30] A. Aghajani, C. Somsen, G. Eggeler, On the effect of long-term creep on the microstructure of a 12% chromium tempered martensite ferritic steel, Acta Mater. 57 (2009) 5093–5106.
[31] M.P. Sello, W.E. Stumpf, Laves phase embrittlement of the ferritic stainless steel type AISI 441, Mater. Sci. Eng. A 527 (2010) 5194–5202.
[32] S. Benum, E. Nes, Effect of precipitation on the evolution of cube recrystallization texture, Acta Mater. 45 (1997) 4593–4602.
[33] A. Nadai, Theory of Flow and Fracture of Solids, vol. 1, McGraw-Hill, New York, 1950 297.
[34] A.H. Cottrell, B.A. Bilby, Proc. Phys. Soc. Lond. 62A (1949) 49.
[35] R.K. Ray, J.J. Jonas, R.E. Hook, Cold rolling and annealing textures in low carbon and extra low carbon steels, Int. Mater. Rev. 39 (1994) 129–172.
[36] D. Raabe, K. Lücke, Textures of ferritic stainless steels, Mater. Sci. Technol. 9 (1993) 302–312.
[37] L.A.I. Kestens, H. Pirgazi, Texture formation in metal alloys with cubic crystal structures, Mater. Sci. Technol. 32 (2016) 1303–1315.
[38] T. Haratani, W.B. Hutchinson, I.L. Dillamore, P. Bate, Contribution of shear banding to origin of Goss texture in silicon iron, Metal Science 18 (1984) 57–65.
[39] R.D. Doherty, Recrystallization and texture, Prog. Mater. Sci. 42 (1997) 39–58.
[40] M.-Y. Huh, O. Engler, Effect of intermediate annealing on texture, formability and ridging of 17%Cr ferritic stainless steel sheet, Mater. Sci. Eng. A 308 (2001) 74–87.
[41] L. Hui-Hu, H.-K. Guo, L. Yi, Z.-G. Liu, W.-Q. Li, J.-C. Li, W. Liang, Microstructural evolution, precipitation and mechanical properties of hot rolled 27Cr–4Mo–2Ni ferritic steel during 800 °C aging, Mater. Des. 160 (2018) 999–1009.
[42] M.Z. Quadir, B.J. Duggan, A microstructural study of the origins of γ recrystallization textures in 75% warm rolled IF steel, Acta Mater. 54 (2006) 4337–4350.

[43] S. Takajo, C.C. Merriman, S.C. Vogel, D.P. Field, In-situ EBSD study on the cube texture evolution in 3 wt% Si steel complemented by ex-situ EBSD experiment — from nucleation to grain growth, Acta Mater. 166 (2019) 100–112.
[44] H. Jun-ichi, O. Naoto, I. Hirofumi, Effect of texture on r-value of ferritic stainless steel sheets, ISIJ Int. 51 (2011) 1740–1748.
[45] G.I. Taylor, Plastic strain in metals, J. Inst. Met. 62 (1938) 307–324.
[46] J.F.W. Bishop, R. Hill, XLVI, a theory of the plastic distortion of a polycrystalline aggregate under combined stresses, Philos. Mag. 42 (1951) 414–427.
[47] J.F.W. Bishop, R. Hill, CXXVIII, a theoretical derivation of the plastic properties of a polycrystalline face-centred metal, Philos. Mag. 42 (1951) 1298–1308.
[48] I. Samajdar, B. verlinden, P. Van Houtte, D. Vanderschueren, γ-Fibre recrystallization texture in IF-steel: an investigation on the recrystallization mechanisms, Mater. Sci. Eng. A 238 (1997) 343–350.
[49] R.L. Every, M. Hatherly, Oriented nucleation in low-carbon steels, Texture 1 (1974) 183–194.
[50] D. 'e Dorner, S. Zaefferer, D. Raabe, Retention of the Goss orientation between microbands during cold rolling of an Fe3%Si single crystal, Acta Mater. 55 (2007) 2519–2530.
[51] T. Haratani, W.B. Hutchinson, I.L. Dillamore, P. Bate, Contribution of shear banding to origin of Goss texture in silicon iron, Metal Science 18 (1984) 57–65.
[52] M.Z. Quadir, B.J. Duggan, Deformation banding and recrystallization of a fibre components in heavily rolled IF steel, Acta Mater. 52 (2004) 4011–4021.
[53] A. Kelly, R.B. Nicholson, Strengthening Methods in Crystals, Elsevier publishing company, 1971.
[54] J. Takahashi, K. Kawakami, J. Hamada, K. Kimura, Direct observation of niobium segregation to dislocations in steel, Acta Mater. 107 (2016) 415–422.
[55] V. Kuzucu, M. Aksoy, M.H. Korkut, M.M. Yldlrlm, The effect of niobium on the microstructure of ferritic stainless, Mater. Sci. Eng. A 230 (1997) 75–80.
[56] S.S. Hansen, J.B.V. Sande, M. Cohen, Niobium carbonitride precipitation and austenite recrystallization in hot-rolled microalloyed steels, Metall. Trans. A. 11 (1980) 387–402.
[57] ASTM, Standard Test Methods for Determining Average Grain Size, E112–12, ASTM International, West Conshohocken, PA, 2012.
[58] P.A. Manohar, M. Ferry, T. Chandra, Five decades of the zener equation, ISIJ Int. 38 (1998) 913–924.
[59] G.E. Dieter, Mechanical Metallurgy, vol. 3, McGraw-hill, New York, 1986.
[60] M. Fukuhara, A. Sanpei, Elastic moduli and internal friction of low carbon and stainless steels as a function of temperature, ISIJ Int. 33 (1993) 508–512.
[61] S. Ratanaphan, D.L. Olmsted, V.V. Bulatov, E.A. Holm, A.D. Rollett, G.S. Rohrer, Grain boundary energies in body-centered cubic metals, Acta Mater. 88 (2015) 346–354.
[62] A.F. Padilha, I.F. Machado, R.L. Plauta, J. Mater. Process. Technol. 170 (2005) 89–96.
[63] M. Akita, Y. Uematsu, T. Kakiuchi, M. Nakajima, Y. Nakamura, Procedia Mater. Sci. 3 (2014) 517–523.
[64] N.J. Petch, The ductile-brittle transition in the fracture of a-iron I, Philos. Mag. 8 (1958) 1089–1097.
[65] A.C.T.M. Zwieten, Some considerations on the toughness properties of ferritic stainless steels—a brief review, Int. J. Press. Vessel. Pip. 56 (1993) 1–31.
[66] N. Fujita, K. Ohmura, M. Kikuchi, Expressions for solubility products of Fe_3Nb_3c carbide and Fe_2Nb laves phase in niobium alloyed ferritic stainless steels, ISIJ Int. 43 (12) (2003) 1999.
[67] Z.Y. Liu, F. Gao, L.Z. Jiang, G.D. Wang, The correlation between yielding behavior and precipitation in ultra purified ferritic stainless steels, Mater. Sci. Eng. A 527 (2010) 3800–3806.